Dalton Transactions

Design of Novel Lanthanide-Doped Core-Shell Nanocrystals with Dual Up-conversion and Down-conversion Luminescence for Anti-counterfeiting Printing

Journal:	*Dalton Transactions*
Manuscript ID	DT-ART-03-2019-001298.R1
Article Type:	Paper
Date Submitted by the Author:	14-Apr-2019
Complete List of Authors:	Xie, Shaowen; Hunan University of Technology Gong, Guo ; Hunan University of Technology Song, Ya; Hunan University of Technology Tan, Haihu; Hunan University of Technology Zhang, Changfan; Hunan University of Technology Li, Na; Hunan University of Technology Zhang, Yanxian; University of Akron Xu, Lijian; Hunan University of Technology Xu, Jianxiong; Hunan University of Technology Zheng, Jie; University of Akron

Design of Novel Lanthanide-Doped Core-Shell Nanocrystals with Dual Up-conversion and Down-conversion Luminescence for Anti-counterfeiting Printing†

Shaowen Xie,[a,c#] Guo Gong,[a#] Ya Song,[a] Haihu Tan,[a] Changfan Zhang,[a] Na Li [a,b,d] Yanxian Zhang,[c] Lijian Xu,[a,b,d] Jianxiong Xu,[a,b,d] and Jie Zheng[c]*

[a]Hunan Key Laboratory of Biomedical Nanomaterials and Devices, College of Life Science and Chemistry, Hunan University of Technology, Zhuzhou 412007, P. R. China

[b]National & Local Joint Engineering Research Center of Advanced Packaging Materials Developing Technology, Hunan University of Technology, Zhuzhou, 412007, PR China

[c]Department of Chemical and Biomolecular Engineering, The University of Akron, Akron, OH, 44325, USA

[d]School of Materials Science and Energy Engineering, Foshan University, Foshan, 528000, P. R. China

† Electronic supplementary information (ESI) available.

[#]Joint first authors, contributed equally to this work.

* To whom correspondence should be addressed. E-mail: (J.X.) xujianxiong8411@163.com

Abstract: Development of advanced luminescent nanomaterials and technologies is of great significance for anti-counterfeiting applications in global economy, security, and human health, but has proved to be a great challenge. In this work, we design, synthesize, and characterize mono-dispersed, dumbbell-shaped lanthanide-doped $NaYF_4$@$NaGdF_4$ core-shell nanoparticles (CSNPs) with dual-mode fluorescence by coating $NaGdF_4$:Ln'^{3+} shell onto $NaYF_4$:Ln^{3+} core nanospheres via a two-step oleic acid mediated thermal decomposition process. Different from conventional synthesis method to produce spherical nanoparticles, the epitaxial growth of $NaGdF_4$:Ln'^{3+} shell onto the nanosphere cores and the lattice mismatch between β-$NaGdF_4$ and β-$NaYF_4$ nanocrystals enable the formation of dumbbell-shaped CSNPs, as evidenced by the morphological evolution of CSNPs and as explained by the Ostwald ripening growth mechanism. By tailoring different doped lanthanide ions in the core and the shell, the resultant CSNPs exhibit tunable but different up-/down-conversion luminescence under the irradiation of a 980 nm laser and a 254 nm UV light, respectively. Finally, these hydrophilic CSNPs are further fabricated into environmental benign luminescent inks for inkjet printing to create a variety of dual-mode fluorescence patterns (peacock, temple, and a logo of "Hunan University of Technology") on different paper-based substrates (A4 paper, envelope, and postcard). Our dual-mode light-responsive CSNPs, along with an easy fabrication method, provide a simple and promising materials and technique for anti-counterfeiting applications.

Keywords: dual-mode luminescent, lanthanide-doped ions, core-shell nanoparticles, inkjet printing, anti-counterfeiting

1. Introduction

Next-generation anti-counterfeiting technologies have placed a great and growing demand in global economy, security, and human health.[1-3] It is estimated that counterfeiting products create multi-billion-dollars illegal profits annually. During the past decades, a wide variety of anti-counterfeiting technologies, including radio frequency identification (RFID),[4] laser holography,[5] nuclear trackers,[6] and bar codes,[7-8] have been developed to combat counterfeiting. However, most of these anti-counterfeiting technologies are relatively well-known and readily hacked by the counterfeiters. From a materials point of view, luminescence materials and their corresponding anti-counterfeiting technologies are highly promising, simply because of their diverse chemical, optical properties, high security characteristics and difficulty for duplication.[9-11] In particular, both down-conversion (DC) luminescent nanomaterials such as quantum dots (QDs),[12,13] carbon dots (CDs),[14,15] metal-organic frameworks (MOFs)[16-18] and up-conversion (UC) luminescent nanomaterials[19-22] are emerging as attractive materials, because these UC and DC luminescent materials possess unique features of high fluorescence intensity, high stability, and ease of handling. More importantly, these materials can be readily fabricated into luminescent inks for printing-based anti-counterfeiting applications, such as stamp printing,[23] screen printing[24] and inkjet printing.[25,26]

Among different printing-based anti-counterfeiting techniques, inkjet printing of UC and DC luminescent materials is the most popular method capable for directly and easily fabricating large-scale, complex, high resolution optical patterns.[27] Significant efforts and progresses have been made to achieve anti-counterfeiting by inkjet printing lanthanide doped luminescent nanomaterials. It is well-known that as compared to other luminescent materials (organic fluorescent dyes, quantum dots, plasmonic materials), the lanthanide ions (Ln^{3+})-doped

nanomaterials possess many advantages including sharp emission peaks, long fluorescence lifetime, low long-term toxicity and superior photostability, making them good candidate for diverse optical applications.[28-29] More importantly, the lanthanide ions (Ln^{3+})-doped nanomaterials have ability to change their colors in response to different wavelengths ranging from UV-vis to NIR spectral region depending on doping ions and host materials.[30-32]

Generally speaking, the lanthanide-doped luminescent nanomaterials for anti-counterfeiting can be classified into single-mode and dual-mode luminescent materials. Single-mode luminescent materials, including either UC or DC luminescent materials, can exhibit different color outputs by using different rare-earth ions (Er, Tm, Ho, Nd), tuning their ion concentration, and/or constructing different nanostructures.[33-36] However, traditional single-mode luminescent anti-counterfeiting materials can still be duplicated easily. So, the fabrication of dual-mode anti-counterfeiting inks by combining both DC and UC luminescent materials has been recently proposed, and several dual-mode UC/DC materials have been realized by a simple mixing of DC and UC luminescent materials together to produce dual-mode luminescence inks for inkjet printing.[37-43] These mixed UC/DC luminescent materials include Gd_2O_3:Yb^{3+}/Er^{3+}/$Eu(DBM)_3Phen$,[38] $Gd_{1.7}Yb_{0.2}Er_{0.3}O_3/Zn_{0.98}Mn_{0.02}S$,[39] $NaYF_4$:Er,Yb(Tm)/carbon dots,[40] $NaYF_4$:Yb,Er@$NaYF_4$@$mSiO_2$-$[Ru(dpp)_3]_2^+Cl_2$ complex,[41] and oleic acid-stabilized lanthanide-doped $NaYF_4$ nanocrystals.[42] All these simple mixtures of UC/DC nanocomposite inks are capable for displaying distinct UC fluorescence under a 980 nm laser and DC fluorescence under a UV lamp. However, this method was time-consuming, process-tedious, and difficult to control the spatial distribution of UC and DC materials, because the DC and UC luminescent materials need to be synthesized separately. Also, this simple mixture strategy suffers from a stability issue to produce the robust, dual-mode luminescence anti-counterfeiting inks.

In order to yield stable dual-mode luminescence, a better strategy is to integrate both DC and UC materials into a single nanostructure. A number of studies have reported different dual-mode luminescent materials by doping multiple UC and DC lanthanide-based activators onto the same nanoparticles as hosting materials such as Y_2O_3,[43] Ba_2GdF_7/Ba_2GdF_5,[44] and $NaREF_4$.[45] Among them, rare earth fluorides with a general formula $NaREF_4$ (RE = Y, Sc, and La-Lu) have been recognized as one of the most commonly used host materials for the doping of lanthanide ions to achieve both DC and UC luminescence, due to their high chemical stability and low-energy photon.[46-48] However, simultaneous incorporation of two visible emitting ions in a single counterpart of lanthanide doped UC nanostructures usually presented low UC fluorescence due to the weak inter-ion electronic coupling between rare earth ions. In principle, the design of the proper core-shell nanostructures for separating UC and DC rare earth ions into different layers is a workable strategy to achieve efficient dual-mode luminescence in a single nanostructure.[49-51] Chen *et al.*[50] designed a novel strategy to fabricate *β*-$NaGdF_4$ nanocrystals consisting of a $NaGdF_4$:Yb,Tm core and $NaGdF_4$:Eu shell to achieve dual-mode luminescence from identical Eu^{3+} ions. In this core-shell nanostructure, the intense UC luminescence of Eu^{3+} in the shells could be achieved after irradiation at 976 nm laser by taking advantage of the Yb^{3+} and Tm^{3+} ions in the core acting as double sensitizers. In addition, the red DC luminescence of Eu^{3+} could be detected via the sensitization of Gd^{3+} ions under the excitation at 273 nm UV light. Ding *et al.*[51] also fabricated dual-mode fluorescent nanocrystals by coating a $NaGdF_4$:Ce,Tb shell with DC emission on the surface of UC nanoparticles of $NaGdF_4$:Yb/Tm. Although significant progresses have been made in synthesis of nanocrystals with dual-mode luminescence, the application of these core-shell nanoparticles in anti-counterfeiting is still limited. Two challenges account for this limitation. First, it is difficult to obtain pre-determined fluorescent color from the abovementioned core-shell

structures via the energy transfer process from sensitizer to activator. Secondly, the produced luminescent color from the core-shell nanoparticles has a very narrow color gamut. Therefore, the synthesis of dual-mode core-shell nanocrystals with tunable UC and DC fluorescent colors is urgently needed in the anti-counterfeiting fields.[52]

In this work, we synthesized lanthanide-doped $NaYF_4$@$NaGdF_4$ nanoparticles (CSNPs) with a core-shell structure by growing an $NaGdF_4$:Ln'^{3+} layer on the surface of $NaYF_4$:Ln^{3+} *via* the two-steps oleic acid mediated thermal decomposition process. Based on this core-shell structural design, different CSNPs ($NaYF_4$:Ln^{3+}@$NaGdF_4$:Ln'^{3+} (Ln^{3+}=Yb/Er, Yb/Tm and Er/Tm, Ln'^{3+}=Ce/Eu, Ce/Tb and Ce/Dy) can be obtained by tailoring the type and concentration of dopants to achieve with dual-mode fluorescence of high intensity, i.e. tunable UC emission colors (RGB colors) from the $NaYF_4$:Ln^{3+} core under near-infrared light of 980 nm and DC emission colors (RGB colors) from the $NaGdF_4$:Ln'^{3+} under ultraviolet light of 254 nm. The resultant CSNPs were further fabricated into luminescent inks for producing various luminescent patterns on different paper-based substrates via inkjet printing. This work demonstrates a new simple strategy to prepare environment-friendly luminescent inks with dual-mode light-responsive ability and high concealment for anti-counterfeiting applications.

2. Experimental

2.1. Chemicals and materials

$YCl_3 \cdot 6H_2O$ (99.9%), $YbCl_3 \cdot 6H_2O$ (99.9%), $ErCl_3 \cdot 6H_2O$ (99.9%), $TmCl_3 \cdot 6H_2O$ (99.9%), $GdCl_3 \cdot 6H_2O$ (99.9%), $CeCl_3 \cdot 6H_2O$ (99.9%), $EuCl_3 \cdot 6H_2O$ (99.9%), $TbCl_3 \cdot 6H_2O$ (99.9%), $DyCl_3 \cdot 6H_2O$ (99.9%), *n*-hexane (AR, 97%), ammonium fluoride (NH_4F, AR), sodium hydroxide (NaOH, AR) were purchased from Shanghai Aladdin Chemistry Co., Ltd. (China). Oleic acid (OA,

90% technical grade) and 1-octadecene (ODE, 90% technical grade) were purchased from Sigma-Aldrich. Sodium oleate (>97.0%) was obtained from TCI. Deionized (DI) water was used during the entire experimental process. All chemical reagents were used without any purification.

2.2. Synthesis of lanthanide oleate ($Ln(oleate)_3$) complexes

The $Ln(oleate)_3$ complexes were prepared by mixing rare-earth chloride with sodium oleate as discussed elsewhere.[53] In a typical synthesis for $Y_{0.78}Yb_{0.20}Er_{0.02}$-oleate complexes, 0.4732 g (1.56 mmol) YCl_3, 0.1549 g (0.40 mmol) $YbCl_3$, 0.0158 g (0.04 mmol) $ErCl_3$ and 1.8570 g (6.1 mmol) sodium oleate were added into a three-necked flask containing a solvent mixture of deionized water (6 mL), ethanol (7 mL) and *n*-hexane (14 mL). The molar ratio of Y:Yb:Er was kept at 78:20:2. The solution was stirred at room temperature for 0.5 h and then transformed to a preheated water-bath of 70 °C. The whole reaction system was maintained at 70 °C for 4 h with vigorous stirring. After the complement of the reaction, the upper oil phase containing $Y_{0.78}Yb_{0.20}Er_{0.02}$-oleate complexes were washed three times with DI water (20 mL × 3) to remove the byproduct of NaCl. Subsequently, hexane was evaporated off under vacuum, resulting in $Y_{0.78}Yb_{0.20}Er_{0.02}$-oleate complexes in a waxy solid form. The preparation of $Y_{0.747}Yb_{0.25}Tm_{0.003}$-oleate complexes, $Y_{0.88}Er_{0.10}Tm_{0.02}$-oleate complexes, $Gd_{0.85}Ce_{0.10}Eu_{0.05}$-oleate complexes, $Gd_{0.85}Ce_{0.10}Tb_{0.05}$-oleate complexes, $Gd_{0.85}Ce_{0.10}Dy_{0.05}$-oleate complexes were similar to that of $Y_{0.78}Yb_{0.20}Er_{0.02}$-oleate complexes just by the alteration of doping categories and molar ratio.

2.3. Synthesis of $NaYF_4$:Ln^{3+} (Ln^{3+} = Yb/Er, Yb/Tm and Er/Tm) core UCNPs

$NaYF_4$:Ln^{3+} core UCNPs were synthesized *via* thermal decomposition strategy employing $Ln(oleate)_3$ complexes as precursors.[54] Herein, we chose the synthesis of $NaYF_4$:20%Yb/2%Er core UCNPs (denoted as UCNPs-G) as a typical example. Typically, 2 mmol (1.900 g) of

$Y_{0.78}Yb_{0.20}Er_{0.02}$-oleate complexes were mixed with 12 mL OA and 30 mL ODE in a three-necked flask at room temperature with vigorous stirring. The solution was degassed, and heated to 140 °C to form a transparent solution, and then cooled down to 50 °C. Subsequently, a methanol solution (20 mL) containing NaOH (0.2000 g, 5.0 mmol) and NH_4F (0.2963 g, 8.0 mmol) was added to the reaction flask and the formed colloidal solution was stirred for 1 h. After that, methanol in the reaction system was removed by heating and degassing the solution at 110 °C for 30 min. The reaction mixture was then heated to 310 °C and maintained for 1.5 h under argon atmosphere. After the completement of the reaction, the reaction system was cooled down naturally and the resultant solution was precipitated in 40 mL ethanol. The UCNPs were collected by centrifugation (14000 rpm, 10 min) and washed with 80 mL ethanol/cyclohexane (4:1) mixture for three times. The as-prepared UCNPs were finally redispersed in 10 mL of cyclohexane for the subsequent use. Similarly, $NaYF_4$:25%Yb/0.3%Tm and $NaYF_4$:10%Er/2%Tm UCNPs denoted as UCNPs-B and UCNPs-R, respectively, were prepared using the same procedures and employing $Y_{0.747}Yb_{0.25}Tm_{0.003}$-oleate complexes and $Y_{0.88}Er_{0.10}Tm_{0.02}$-oleate complexes as precursors, respectively.

2.4. Synthesis of $NaYF_4:Ln^{3+}@NaGdF_4:Ln'^{3+}$ (Ln'^{3+} = Ce/Eu, Ce/Tb and Ce/Dy) CSNPs

The synthesis of $NaYF_4:Ln^{3+}@NaGdF_4:Ln'^{3+}$ CSNPs were achieved by growing $NaGdF_4:Ln'^{3+}$ shell on the surface of $NaYF_4:Ln^{3+}$ nanocrystal through thermal decomposition method. Taken the synthesis of $NaYF_4$:20%Yb/2%Er@$NaGdF_4$:10%Ce/5%Eu CSNPs (denoted as CSNPs-GR) as a typical example, 2 mmol (2.0 g) of $Gd_{0.85}Ce_{0.10}Eu_{0.05}$-oleate complexes were mixed with 12 mL OA and 30 mL ODE in a three-necked flask at room temperature with vigorous stirring. The mixture solution was heated to 140 °C and continuously stirred to form a transparent solution, and then cooled down to 80 °C. Subsequently, 10 mL of cyclohexane containing 0.3 g

the above synthesized UCNPs-G was added in the mixture solution and stirred for 10 min. After that, the cyclohexane was removed by maintaining the mixture solution at 80 °C under vacuum for 30 min and then the resultant solution was cooled down to 50 °C. A methanol solution (20 mL) containing NaOH (0.2000 g, 5.0 mmol) and NH_4F (0.2963 g, 8.0 mmol) was added to the reaction flask, stirred for 1 h and followed evaporation of methanol by degassing the solution at 100 °C for 30 min. The reaction mixture was then heated to 310 °C and maintained for 1.5 h under argon atmosphere. After the completion of the reaction, the reaction system was cooled down to room temperature and the resultant solution was precipitated in 40 mL ethanol. The resultant CSNPs-GR sample was collected by centrifugation (14000 rpm, 10 min), washed with 80 mL ethanol/cyclohexane (4:1) mixture for three times. The as-prepared CSNPs were finally redispersed in 10 mL of cyclohexane for the subsequent use. Moreover, $NaYF_4$:25%Yb/0.3%Tm@$NaGdF_4$:10%Ce/5%Tb CSNPs and $NaYF_4$:10%Er/2%Tm@$NaGdF_4$:10%Ce/5%Dy CSNPs were prepared using the corresponding $Ln(oleate)_3$ complexes and $NaYF_4$:Ln^{3+} core UCNPs, respectively. The other two samples were denoted as CSNPs-BG and CSNPs-RB, respectively. For example, $NaYF_4$:25%Yb/0.3%Tm@$NaGdF_4$:10%Ce/5%Tb CSNPs (CSNPs-BG) could be obtained by using $Gd_{0.85}Ce_{0.10}Tb_{0.05}$-oleate complexes and $NaYF_4$:25%Yb/0.3%Tm core UCNPs. Similarly, $NaYF_4$:10%Er/2%Tm@$NaGdF_4$:10%Ce/5%Dy CSNPs (CSNPs-RB) could be obtained by using $Gd_{0.85}Ce_{0.10}Dy_{0.05}$-oleate complexes and $NaYF_4$:10%Er/2%Tm core UCNPs.

2.5. Surface modification of CSNPs

In order to obtain water-dispersible ligands-free CSNPs, a simple acid treatment process was employed to remove the OA ligands from the surface of CSNPs.[55] Typically, 10 mL cyclohexane solution containing 0.6 g CSNPs were precipitated by the addition of ethanol, collected by

centrifugation (14000 rpm, 10 min) and redispersed in 10 mL HCl solution (0.1 M in deionized water) to form a slurry. The slurry was then sonicated at 45 °C for 1 h to remove the OA ligands. After that, the ligands-free CSNPs were collected via centrifugation at 14000 rpm for 20 min, washed twice with deionized water (2 × 5 mL) and dried under vacuum at 60 °C for 12 h.

2.6. Formulation of dual-mode luminescent CSNPs inks

The dual-mode luminescent CSNPs inks were prepared by dispersing the ligands-free CSNPs in a mixture solvent of ethanol, water and glycerol. Typically, a certain amount of CSNPs was added to 10 mL mixture solvent. To obtain inks with optimal viscosity and surface tension, the weight ratio of ethanol, water and glycerol was kept at 2:2:1. Afterwards, the resulting mixture was vigorously stirred for 20 min and ultrasonically vibrated for 10 min to achieve well dispersed CSNPs. To produce different dual-mode luminescent inks with similar perceived luminescent brightness, the contents of CSNPs-GR, CSNPs-BG and CSNPs-RB in dual-mode luminescent inks were kept at 0.20 wt%, 0.80 wt% and 1.0 wt%, respectively.

2.7. Characterization of different NPs

The phase purity and crystallinity of the as-prepared NPs were characterized by X-ray diffraction (XRD) using a Rigaku Model D/max-2500 diffractometer, with Cu Kα radiation in the 2θ range of 10-80° with a step size of 0.02°. Fourier transform infrared spectroscopy (FT-IR) was recorded on a Nicolet 380 spectrometer using 32 scans and a 4 cm^{-1} resolution. Thermogravimetric analysis (TGA) performed in nitrogen atmosphere using a Q-50 apparatus at 10 °C/min heating rate from the room temperature to 600 °C for the samples. Transmission electron microscopy (TEM) analysis, high-resolution TEM (HR-TEM) and scanning transmission electron microscopy (STEM) was performed on a JEM-1011 instrument operating at an accelerating voltage of 100 kV.

X-ray photoelectron spectroscopy (XPS) spectra were obtained with a PHI 5000 Versa Probe system, using a monochromatic Al Kα X-ray source. The fluorescence spectra of the nanoparticles were carried out using a Hitachi F-4600 fluorescence spectrophotometer equipped with an external CNI (2W) 980 nm IR Fiber coupled laser system (Changchun New Industries Optoelectronics Tech. Co., Ltd). The luminescent digital photographs under NIR and UV irradiation were obtained using a Nikon D7000 camera with an UV/IR cuter. The excitation light source for obtaining the down-conversion luminescent images was a ZF-1A UV analyzer with three types of light (365 nm, 254 nm and white light). The inkjet printing of the CSNPs inks was performed on a Canon PIXMA ip2780 inkjet printer equipped with 25-pL cartridge (PG-815). The PG-815 cartridge that was capable of generating inks droplets as small as about 36 μm in diameter was the experimental cartridge.

3. Results and discussion

Scheme 1 briefly presented a general procedure for the synthesis and inkjet printing of $NaYF_4:Ln^{3+}@NaGdF_4:Ln'^{3+}$ CSNPs for anti-counterfeiting patterns. Firstly, we synthesized oleic acid (OA) ligands functionalized $NaYF_4:Ln^{3+}@NaGdF_4:Ln'^{3+}$ CSNPs (OA-CSNPs) by growing an $NaGdF_4:Ln'^{3+}$ layer on the surface of $NaYF_4:Ln^{3+}$ *via* a sequential two-step OA-mediated thermal decomposition process, similar to the procedure as reported for synthesis of $NaYF_4@NaYF_4$ core-shell nanoparticles.[56] During this process, the $NaYF_4:Ln^{3+}$ core UCNPs were first synthesized, and then served as the seed crystals for the growth of a $NaGdF_4$ shell in the presence of oleic acid (OA) and 1-octadecene. After that, the OA ligands were removed from the surface of OA-CSNPs by a simple acid treatment process, yielding hydrophilic ligand-free CSNPs. Secondly, we dispersed the ligand-free CSNPs into a mixture solvent of ethanol, deionized water

and glycerol to produce environmental benign dual-mode luminescent CSNPs inks. Finally, we used the dual-mode luminescent CSNPs inks to create anti-counterfeiting patterns on different paper-based substrates by inkjet printing. The constructed anti-counterfeiting patterns was invisible in visual light, but displayed bright UC luminescence (green, blue, or red=RGB colors) under 980 nm NIR light and distinct DC luminescence (RGB colors) with 254 nm UV light.

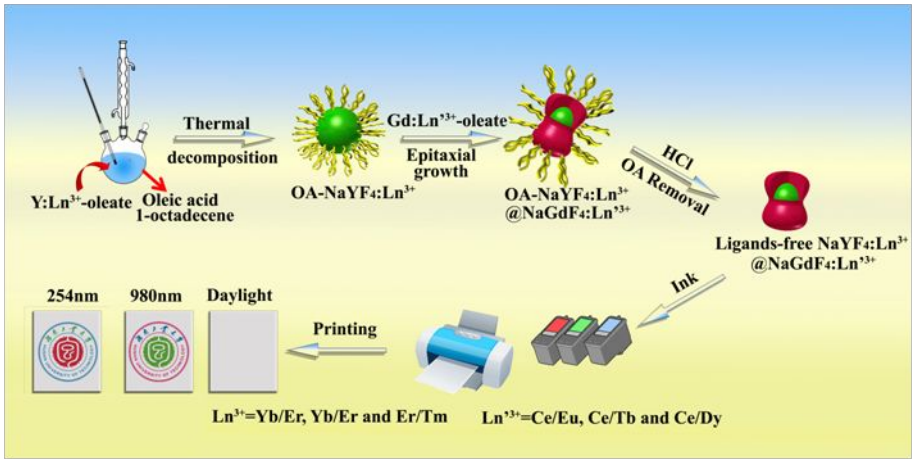

Scheme 1. Schematic representation of the synthesis and inkjet printing of the dual-mode $NaYF_4:Ln^{3+}@NaGdF_4:Ln'^{3+}$ CSNPs for creating paper-based anti-counterfeiting patterns.

To confirm the core-shell structure of as-obtained CSNPs, we comparatively examined the structure, morphology, composition, and optical properties of UCNPs-G ($NaYF_4$:20%Yb/2%Er) and CSNPs-GR ($NaYF_4$:20%Yb/2%Er@$NaGdF_4$:10%Ce/5%Eu) nanoparticles using XRD, XPS, and TEM. **Fig. 1** shows the XRD patterns of UCNPs-G and CSNPs-GR. It can be seen that all XRD peaks in UCNPs-G were well indexed and consistent with the standard pattern of hexagonal-phase $NaYF_4$ (JCPDS: 16-0334), and no other phases were observed. This indicates that the formation of pure β-$NaYF_4$ nanocrystals as a core structure in UCNPs-G. Upon the coating of $NaGdF_4$ shell, all diffraction peaks of CSNPs-GR at 17.10º, 29.87º, and 30.66º, corresponding to the core structure, were still presented and similar to those of UCNPs-G core. In addition, β-$NaYF_4$

nanocrystals (JCPDS: 16-0334) had the lattice constants of a=5.96 Å, and c=3.53 Å, similar to β-$NaGdF_4$ nanocrystals (JCPDS: 27-0699, a=6.02 Å, and c=3.60 Å), suggesting that β-$NaGdF_4$ can be epitaxial grown on β-$NaYF_4$, though the lattice mismatch of β-$NaGdF_4$ and β-$NaYF_4$ nanocrystals was also observed by deviating crystallographic c parameter of 1.99% the and a parameter of 1.00%, respectively. The intensity ratio between (100) and (110) crystal planes of CSNPs-GR showed a higher value than that of the UCNPs-G core alone, indicating that the growth of the $NaGdF_4$ shell undergoes different pathways and kinetics at different phases.[57]

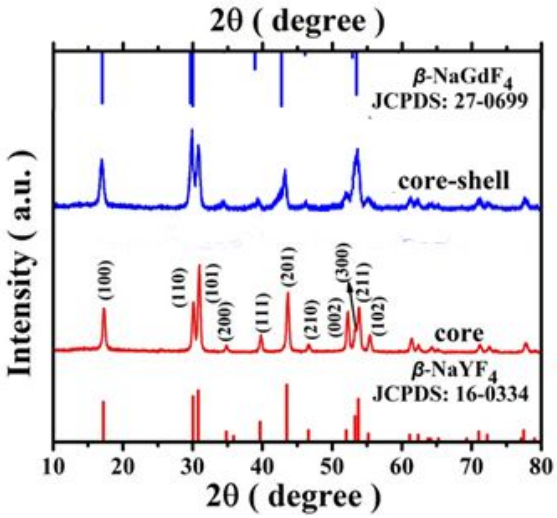

Figure 1. XRD patterns of UCNPs-G (core) and CSNPs-GR (core-shell) in comparison with the standard data of β-$NaYF_4$ (JCPDS No. 16-0334) and β-$NaGdF_4$ (JCPDS No. 27-0699) to confirm the growth of a $NaGdF_4$ shell on the core of $NaYF_4$.

To further confirm that the $NaGdF_4$ shell was coated on $NaYF_4$ core, X-ray photoelectron spectroscopy of UCNPs-G and CSNPs-GR was recorded to comparatively analyze their elemental composition. **Fig. 2A** shows the full XPS spectrum of UCNPs-G and CSNPs-GR, with some observable similarities and differences. First, both UCNPs-G and CSNPs-GR exhibited four strong peaks located at 160.0, 302.0, 685.0, and 1072.0 eV, which were attributed to the binding energies

of Y 3d, Y 3p, F 1s, and Na 1s, respectively. Secondly, UCNPs-G also showed the other three peaks at 285.0, 397.0 and 532.0 eV associated with C 1s, N 1s and O 1s. Besides, the peaks at 186.3 eV for Yb 4d5/2 and 171.9 eV for Er 4d5/2 were also observed, as shown in the magnified XPS spectra in 194~185 eV (**Fig. 2B**) and 173~165 eV (**Fig. 2C**). These XPS results suggested that Yb and Er elements were successfully doped onto the host β-$NaYF_4$ matrix and the nanocrystal core was mainly composed of $NaYF_4$:Yb/Er. Thirdly, different from XPS spectrum of UCNPs-G, CSNPs-GR showed three distinct peaks of Gd 4d (**Fig. 2D**), Ce 3d (**Fig. 2E**), and Eu 3d5/2 (**Fig. 2F**). This was a strong evidence to confirm the formation of $NaYF_4$:Yb/Er and $NaGdF_4$:Ce/Eu composite materials after the epitaxial growth of the $NaGdF_4$:Ce/Eu shell on the $NaYF_4$ core. Moreover, the corresponding intensities of Y 3p, Y 3d, Yb 4d5/2, and Er 4d5/2 peaks were all decreased as compared to those of $NaYF_4$ core. Since the XPS measurement mainly detects the surface elemental composition of materials, the decrease of these peak intensities of $NaYF_4$:Yb/Er potentially suggests the formation of $NaYF_4$:Yb/Er@$NaGdF_4$:Ce/Eu core-shell structure, where $NaGdF_4$:Ce/Eu were deposited on the surface of $NaYF_4$:Yb/Er.

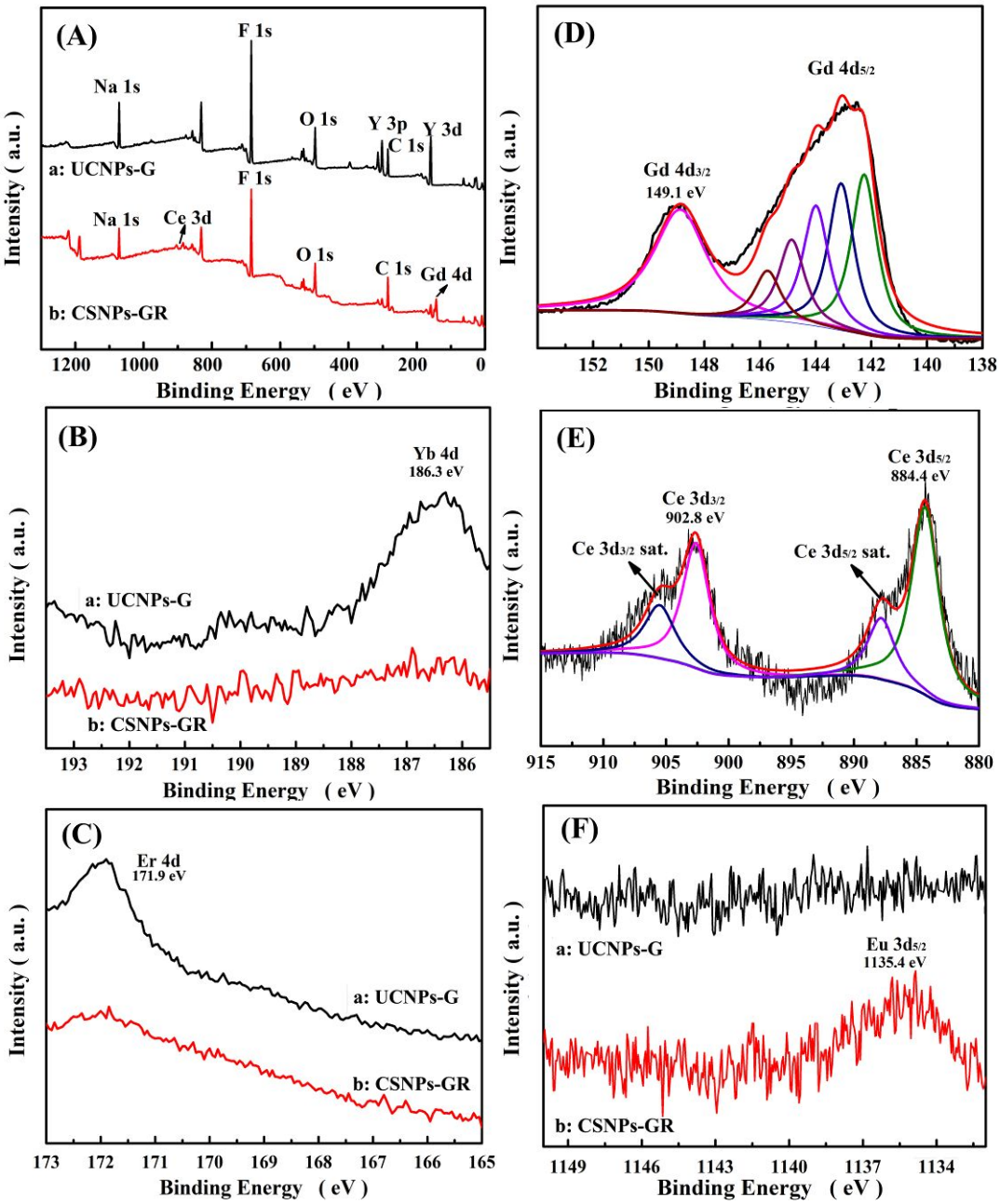

Figure 2. XPS spectra of UCNPs-G and CSNPs-GR, as shown by (A) survey spectra and high-resolution spectra of (B) Yb 4d, (C) Er 4d, (D) Gd 4d, (E) Ce 3d, and (F) Eu 3d.

To test this hypothesis about elemental distributions on the core-shell structure, the as-prepared CSNPs-GR sample was subjected to STEM characterization. In **Fig. 3**, a series of STEM images of the as-prepared CSNPs-GR showed the elemental mapping for Y (green), Yb (purple),

Gd (yellow), and Ce (pink), demonstrating the coexistence of these elements in the as-prepared CSNPs-GR. It was also interesting to observe that Gd and Ce elements were symmetrically distributed at the two edges of the dumbbell, while Y and Yb elements were located in the center of the dumbbell. So, STEM images, in parallel, demonstrate the core-shell structure of the as-prepared CSNPs-GR, consisting of the $NaGdF_4$:Ce/Eu shell and the $NaYF_4$:Yb/Er core.

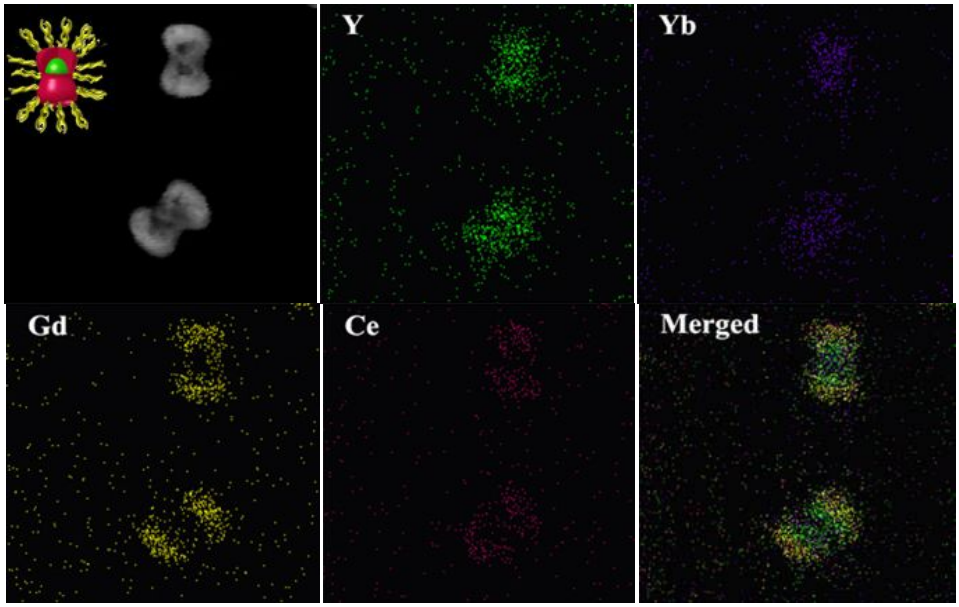

Figure 3. Scanning transmission electron microscopy images of CSNPs-GR (inset: molecular structure of CSNPs-GR obtained from molecular simulations) and different element maps of Gd, Ce, Y, and Yb elements.

During the synthesis process of CSNPs, OA was chosen as capping ligands to control the particle growth and prevent the nanoparticles from aggregation. It is expected that the resultant nanoparticles should be capped with hydrophobic OA ligands on the surface of CSNPs and also be well dispersed in a variety of nonpolar solvents such as cyclohexane.[58] To examine the growth behavior of the $NaGdF_4$ shell on the $NaYF_4$ core, we compared the morphological and optical properties of UCNPs-G and CSNPs-GR in cyclohexane solution. At the first glance in **Fig. 4A$_1$-**

A_3 and **Fig. $4B_1$-B_3**, both as-synthesized UCNPs-G and CSNPs-GR nanoparticles were well dispersed in cyclohexane solution, forming a transparent solution. Upon exposure of both nanoparticles under two wavelength lights, UCNPs-G without a shell coating only exhibited a single-mode green UC luminescence under 980 nm laser irradiation, while CSNPs-GR with a core-shell structure displayed a dual-mode luminescence to emit a UC green color at a 980 nm laser and a DC red color at a 254 nm UV lamp. TEM images also showed that as-prepared UCNPs-G nanoparticles presented fairly mono-dispersed spherical shape, with the average diameter of ~24 nm (**Fig. $4A_4$**) and the lattice fringe *d*-spacing of 0.52 nm (**Fig. $4A_5$**), whose morphological lattice structure is in good agreement with that in the (100) plane of hexagonal-phase $NaYF_4$. Differently, after epitaxial growth of a shell of $NaGdF_4$:10%Ce/5%Eu on the $NaYF_4$:20%Yb/2%Er, the acquired CSNPs-GR nanoparticles displayed a highly uniform dumbbell shape, with the longest length of ~45 nm and the diameter of the two ends of ~34 nm (**Fig. $4B_4$)**. The high-resolution TEM (HR-TEM) image of CSNPs-GR also showed highly similar lattice fringes located at the ends of the dumbbell-shaped nanoparticles with *d*-spacing of 0.32 nm (**Fig. $4B_5$**), which corresponds to the (110) crystal plane of hexagonal-phase $NaGdF_4$. A large difference in lattice fringes between core and shell indicates that the introduction of $NaGdF_4$ indeed induces the preferential growth of the $NaGdF_4$ shell along the [001] direction, resulting in different relative crystal growth rate and different morphology in the core and core-shell growth process. Thus, $NaYF_4$:20%Yb/2%Er@$NaGdF_4$:10%Ce/5%Eu nanoparticles formed a dumbbell core-shell shape due to incomplete shell enclosure, instead of spherical core-shell shape, after the epitaxial growth of the $NaGdF_4$:10%Ce/5%Eu shell on the $NaYF_4$:20%Yb/2%Er core.

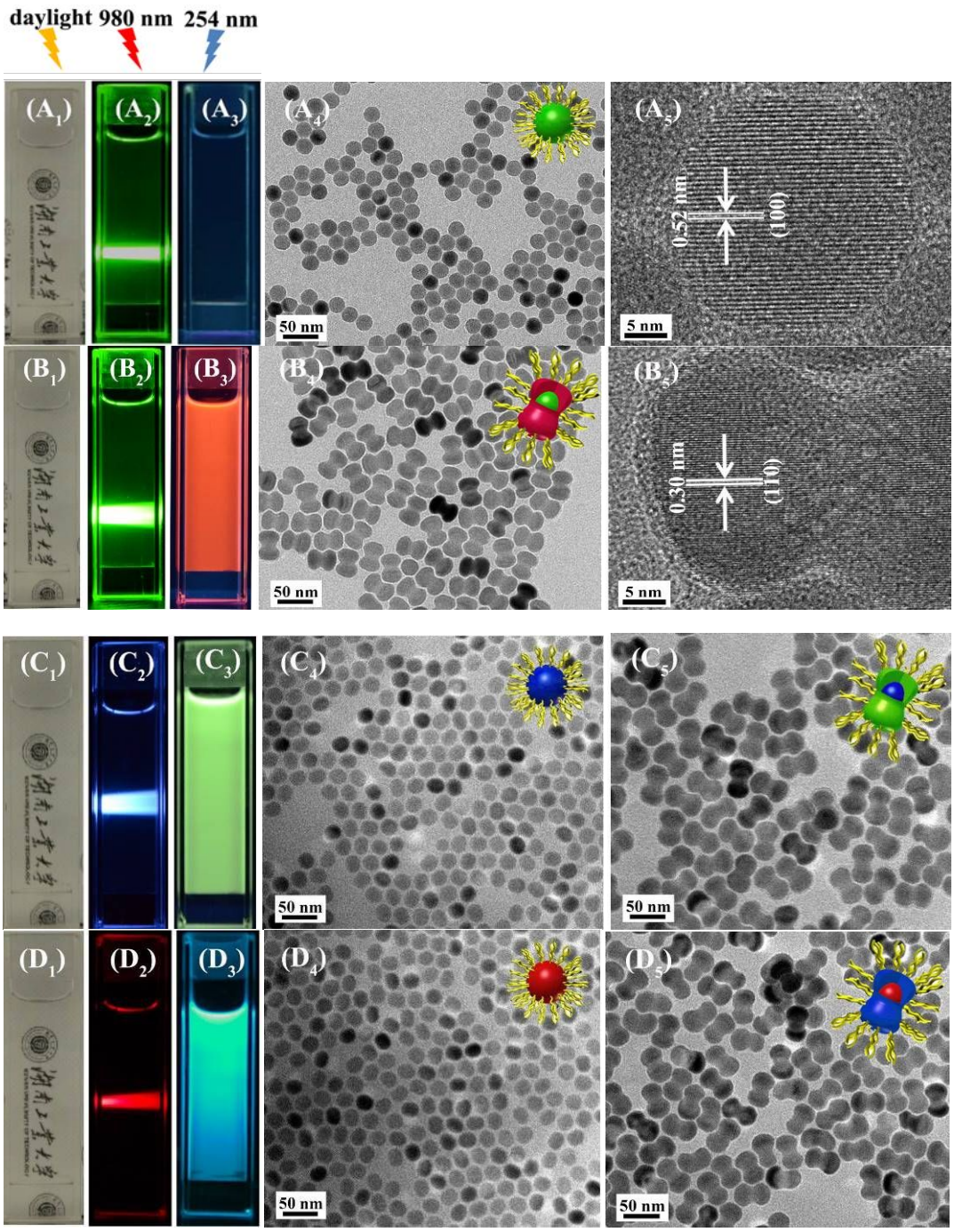

Figure 4. Optical and morphological properties of UCNPs-G, CSNPs-GR, CSNPs-BG, and CSNPs-RB in cyclohexane solution (0.2 wt%). The color emission of UCNPs-G, CSNPs-GR, CSNPs-BG, and CSNPs-RB under daylight (A_1-D_1), UC luminescence at 980 nm laser (A_2-D_2), and DC luminescence at 254 nm UV light (A_3-D_3). TEM images of as-prepared UCNPs-G (A_4),

CSNPs-GR (B_4), UCNPs-B (C_4) and CSNPs-BG (C_5), UCNPs-R (D_4) and CSNPs-RB (D_5). HR-TEM images of UCNPs-G (A_5) and CSNPs-GR (B_5). The corresponding molecular structures determined by molecular modeling were also shown.

To better understand the nanocrystal growth mechanism of CSNPs, a series of CSNPs-GR nanoparticles were synthesized at different times of 0 min, 20 min, 40 min and 90 min and the corresponding time-dependent morphological changes were subjected to TEM characterization. At the beginning of the thermal decomposition process for 0 min, initial UCNPs-G formed spherical shape cores with average diameter of 24 nm (**Fig. 5A**). After 20 min of thermal decomposition reaction, the resultant colloids contained not only the UCNPs-G core but also many small nanoparticles (about 3~5 nm in diameter) (**Fig. 5B**). The formation of the small nanoparticles might be attributed to the homogeneous nucleation of $NaGdF_4$ nanocrystals. As the reaction proceeded, the $NaGdF_4$ nucleus began to aggregate into larger nanocrystals of 8~10 nm in diameters. Since the UCNPs-G core had lower chemical potential, the nanocrystals tended to attach on the surface of UCNPs-G core and thus facilitated the epitaxial growth of a $NaGdF_4$ shell. Due to the lattice mismatch of β-$NaGdF_4$ and β-$NaYF_4$ nanocrystals, the $NaGdF_4$ shell preferred to grow on the two sides of the UCNPs-G spherical core symmetrically, forming dumbbell-shaped core-shell nanocomposites (**Fig. 5C**). After 90 min reaction, all tiny nanoparticles disappeared and were transferred into uniform dumbbell-shaped nanoparticles with the longest length of ~45 nm and two ends diameter of ~34 nm (**Fig. 5D**).

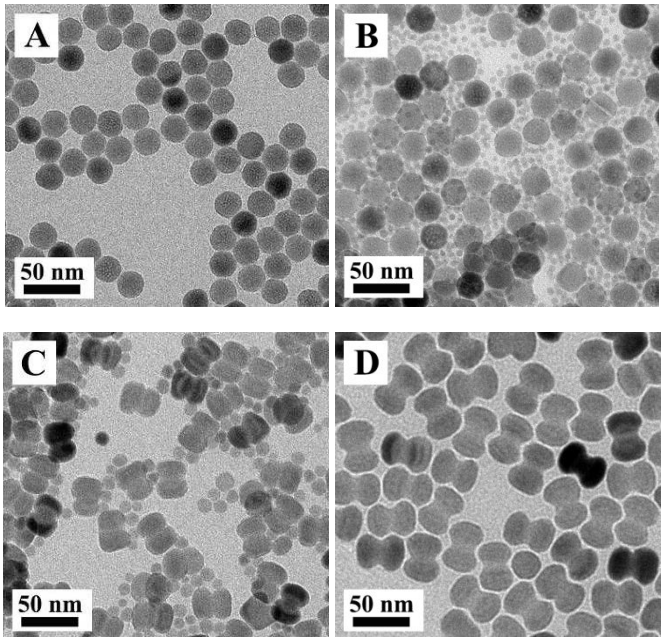

Figure 5. TEM image characterization of morphological changes of CSNPs-GR from (A) spherical nanoparticles at 0 min, to (B) the early intermediate mixtures of spherical nanoparticles and many tiny nanoparticles at 20 min, (C) the later intermediate mixtures of dumbbell-shaped core-shell nanoparticles and less tiny nanoparticles at 40 min, and (D) dumbbell-shaped core-shell nanoparticles at 90 min at 310 °C.

Fig. 6 shows XRD patterns of the CSNPs-GR intermediates obtained at different reaction time intervals. At the beginning of thermal decomposition reaction (t=0 min), the UCNPs-G presented a pure hexagonal phase of $NaYF_4$ (**Fig. 6a**). Upon the thermal decomposition for 20 min, a cubic phase of $NaGdF_4$ (α-$NaGdF_4$) was emerged as evidenced by a diffraction peak at 29.92º (a green cycle) in the presence of hexagonal phase of $NaYF_4$ (**Fig. 6b**). The cubic phase of $NaGdF_4$ is likely attributed by small nanoparticles as observed in **Fig. 5B**. After 40 min of reaction, while the α-$NaGdF_4$ still existed, the β-$NaGdF_4$ phase was observed and the corresponding diffraction peaks at 43.48º were broaden (**Fig. 6c**). Change of diffraction peaks as the reaction was resulted from the combination of β-$NaGdF_4$ and β-$NaYF_4$, in good accordant with TEM images where

small nanoparticles (8~10 nm) and dumbbell-shaped core-shell nanocomposites were observed in **Fig. 5C**. As the thermal decomposition reaction proceeded to 90 min, diffraction peaks only showed the existence of pure hexagonal phase dumbbell-shaped core-shell nanocomposites (**Fig. 6d**).

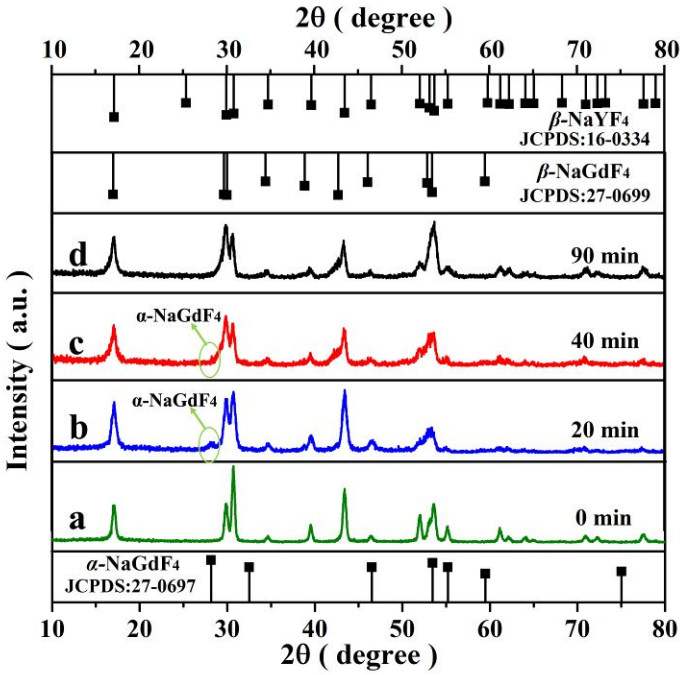

Figure 6. XRD patterns of the intermediates obtained at different reaction time intervals: (a) 0 min, (b) 20 min, (c) 40 min and (d) 90 min, as well as the standard data of α-$NaGdF_4$ (JCPDS No. 27-0697), β-$NaGdF_4$ (JCPDS No. 27-0699) and β-$NaYF_4$ (JCPDS No. 16-0334) phases for comparison.

Both XRD patterns and TEM images suggest that the epitaxial growth of $NaGdF_4$ shell undergo an $\boldsymbol{\alpha \rightarrow \beta}$ phase transformation, accompanied with a morphology evolution from small nanoparticles to a dumbbell-shaped shell. The growth mechanism is driven by the dissolution-nucleation effect, consistent with the classical Ostwald ripening mechanism.[59] At the beginning of thermal decomposition synthesis, α-$NaGdF_4$ particles were first formed, then these α-$NaGdF_4$

nuclei were quickly agglomerated together and grew into the larger α-$NaGdF_4$ spherical nanoparticles. Since these α-$NaGdF_4$ nanoparticles were still thermodynamically unstable, they will be subsequently dissolved to release monomers that in turn were deposited on the core particles of $NaYF_4$ in solution. Such structural transition was caused by the higher solubility of the α-$NaGdF_4$ nanoparticles than the β-phase UCNPs-G cores, leading to the solution being super-saturated by α-$NaGdF_4$ relative to the β-phase particles. Besides, the growth of β-$NaGdF_4$ shell was preferential grown along the preferential (001) direction at the beginning, followed by the growth along (100) and (010) directions, resulted in the formation of dumbbell-like nanostructures.[60]

Doping of different lanthanide ions onto host luminescent materials will produce different UC and DC emissions under UV or NIR irradiation.[61] Here, by tailoring the type and concentration of lanthanide dopants in the $NaYF_4$ core and the $NaGdF_4$ shell separately, different CSNPs with different UC and DC color emission can be obtained. As a proof-of-concept example in **Fig. 4C$_1$-C$_3$**, we achieved dual-mode luminescent properties of $NaYF_4$:25%Yb^{3+}/0.3%Tm^{3+}@$NaGdF_4$:10%Ce/5%Tb^{3+} (CSNPs-BG) in cyclohexane solution, i.e. blue UC emission under 980 nm and green DC emission under 254 nm, by doping (25%Yb^{3+}, 0.3%Tm^{3+}) in the $NaYF_4$ core and (10%Ce^{3+}, 5%Tb^{3+}) in the $NaGdF_4$ shell. Similarly, once we changed the doping formula and doped (10%Er^{3+}, 2%Tm^{3+}) in the $NaYF_4$ core and (10%Ce^{3+}, 5%Dy^{3+}) in the $NaGdF_4$ shell, $NaYF_4$:10%Er^{3+}/2%Tm^{3+}@$NaGdF_4$:10%Ce/5%Dy^{3+} (CSNPs-RB) emitted red light under a 980 nm laser and blue light under a 254 nm UV lamp (**Fig. 4D$_1$-D$_3$**). Both cases demonstrate that doping with different lanthanide ions enables to capture photons over a wide wavelength range and show excellent and diverse optical performance. TEM images in **Fig.**

4C$_5$ and **Fig. 4D$_5$** also showed that both CSNPs-BG and CSNPs-RB nanoparticles presented highly uniform dumbbell-like structure, similar to CSNPs-GR (**Fig. 4B$_4$**).

It is generally accepted that constructing a core-shell structure provides an effective way to improve the UC luminescence of the UCNPs nanoparticles.[62] To validate this point, we compared the UC fluorescence properties of CSNPs-GR with a core-shell structure and UCNPs-G with a sole core structure in cyclohexane under 980 nm laser. As shown in **Fig. 7**, both UCNPs-G and CSNPs-GR exhibited typical UC fluorescent emission peaks of $NaYF_4$:Yb/Er located at the same positions of 408, 521, 541, and 654 nm, which attributed to the transitions of $^2H_{9/2}$-$^4I_{15/2}$, $^2H_{11/2}$-$^4I_{15/2}$, $^4S_{3/2}$-$^4I_{15/2}$ and $^4F_{9/2}$-$^4I_{15/2}$ of Er^{3+}, respectively. But, CSNPs-GR had the higher luminescent intensities than UCNPs-G, probably due to the surface-induced quenching effect of CSNPs-GR that was effectively suppressed after coating the $NaGdF_4$ shell.[63] Besides, for UCNPs-G, upon doping with high concentration of sensitizer ions Yb^{3+} and luminescent center ions Er^{3+}, they were mainly distributed on the surface of UCNPs-G, so that interior ions could transfer excitation energy to the adjacent surface dopant ions, facilitating non-radiative transitions.[64] However, in the case of CSNPs-GR, the dopant ions Yb^{3+} and Er^{3+} were confined to the interior core, so the probability of non-radiative transitions was largely reduced, leading to enhanced UC luminescence of CSNPs-GR upon excitation with NIR light. Such luminescent enhancement phenomenon was also observed for other core-shell systems of CSNPs-BG and CSNPs-RB as compared to the corresponding UCNPs-B (**Fig. 7C**) and UCNPs-R core systems (**Fig. 7E**).

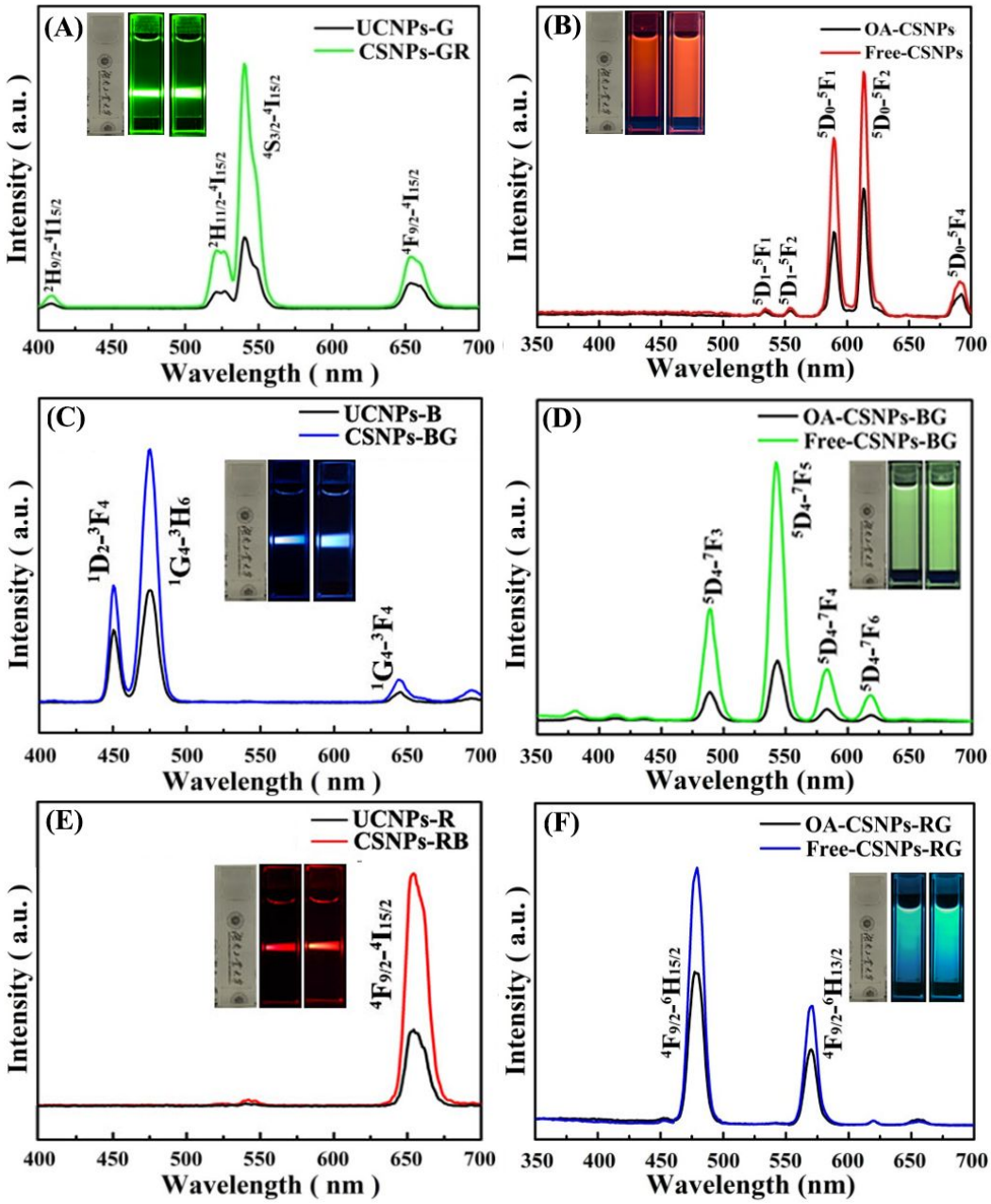

Figure 7. Comparison UC and DC luminescent properties between nanoparticles with and without core-shell structures. UC luminescent spectra of (A) UCNPs-G and CSNPs-GR, (C) UCNPs-B and CSNPs-BG, (E) UCNPs-R and CSNPs-RB. DC luminescent spectra of (B) CSNPs-GR, (D) CSNPs-BG, and (F) CSNPs-RB before and after removal of OA ligands.

To examine the role of the OA ligands in the optical properties of CSNPs, we prepared two types of CSNPs-GR nanocrystals with and without OA ligand coating, namely as OA-CSNPs-GR and free-CSNPs-GR. OA-coated CSNPs-GR (OA-CSNPs-GR) was prepared by the two-step oleic acid mediated thermal decomposition process, while OA-free CSNPs-GR was obtained by a simple acid treatment process to remove the OA. The dispersion experiment showed that the free-CSNPs-GR was well dispersed in water without any observable aggregation (**Fig. S1**). To examine whether OA ligands were completely removed from CSNPs-GR surface, CSNPs-GR before and after acid treatment was subjected to FT-IR analysis. As shown in **Fig. S2A**, the OA-CSNPs-GR exhibited the characteristic peaks of OA molecules before acid treatment. The bands at 2925 and 2858 cm^{-1} were assigned to asymmetric and symmetric stretching vibrations of methylene (CH_2) of the long alkyl chain from the OA ligands, respectively. The peaks at 1718, 1573, and 1452 cm^{-1} were also observed, corresponding to the C=O stretching vibration, the symmetric COO^- (υ_{as}), and the asymmetric COO^- (υ_s) stretches of OA, respectively. After acid treatment, all these five characteristic peaks almost disappeared, indicating the successful removal of OA ligands. To confirm FT-IR observation, TGA analysis was also performed on both OA-CSNPs-GR and free-CSNPs-GR powers. As shown in **Fig. S2B**, upon heating both power samples up to 600 °C, free-CSNPs-GR powder only lost 1.0% in weight in the temperature range of 100 °C to 600 °C, while OA-CSNPs-GR lost ~8.2% in the same temperature range. This indicates that the large weight loss is attributed to the decomposition of the OA capping ligands from the surface of the CSNPs-GR. Since OA ligands would absorb UV light but fail to transfer the energy to lanthanide dopants that will inevitably suppress the DC emission intensity,[65] the removal of OA ligands will lead free-CSNPs-GR to high DC fluorescence signals. In parallel, the photoluminescent spectra of free-CSNPs-GR in water and OA-CSNPs-GR in cyclohexane under 254 nm UV light were compared.

As shown in **Fig. 7B**, excited by 254 nm UV light, both OA-CSNPs-GR and free-CSNPs-GR displayed five emission peaks of Eu^{3+} as activator ion at 534, 554, 589, 613 and 691 nm, corresponding to the transitions of $^5D_1$-$^7F_1$, $^5D_1$-$^7F_2$, $^5D_0$-$^7F_1$, $^5D_0$-$^7F_2$ and $^5D_0$-$^7F_4$ of Eu^{3+}, respectively. It is not surprising to observe that free-CSNPs-GR emitted higher DC florescence intensity than OA-CSNPs-GR. Similar enhanced DC florescence behaviors of free-CSNPs-BG (**Fig. 7D**) and free-CSNPs-RB (**Fig. 7F**) were also observed when comparing with their corresponding OA-coated CSNPs.

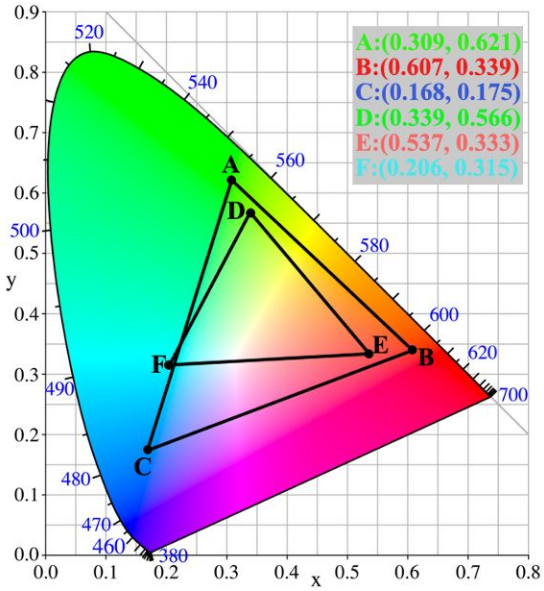

Figure 8. Positions of the upconversion and downconversion emission of CSNPs within the CIE color coordinates. The two triangles connected by A, B and C and by D, E and F indicate the upconversion and downconversion emission of CSNPs, respectively.

Based on the UC and DC luminescent spectra, the color coordinates of the three CSNPs were presented in the Commission Internationale de l'Eclairage (CIE) chromaticity diagram. As shown in **Fig. 8**, the three-primary UC emission color coordinates of CSNPs-GR, CSNPs-RB and CSNPs-BG were (0.309, 0.621), (0.607, 0.339), (0.168, 0.175), and the three-primary DC emission color

coordinates were (0.537, 0.333), (0.206, 0.315), (0.339, and 0.556), respectively. It can be seen that the UC and DC fluorescence of the three CSNPs were mainly located at the red, green and blue region of the chromaticity diagram, confirming that the pre-determined fluorescence color can be readily obtained by the trichromatic additive color theory.

A unique combination of dual-mode responsive fluorescence, tunable luminescent colors, and good water-dispersion ability makes the CSNPs as promising luminescent inks for anti-counterfeiting applications. As a proof-of-concept, we first prepared dual-mode luminescent inks by dispersing ligands-free CSNPs into a mixed solvent of ethanol, water, and glycerol, and then inkjet printed the dual-mode luminescent inks to construct different luminescent-based encryptions on paper substrates for anti-counterfeiting. To implement this idea and ensure the inks being worked stably with an inkjet printer, the ink properties (*i.e.,* dynamic viscosity and surface tension) were carefully tuned by changing the weight ratio of deionized water, ethanol, and glycerol. An optimal weight ratio of ethanol, water and glycerol at 2:2:1 has been demonstrated to produce stable and sensitive CSNPs-GR inks (0.2 wt%), with dynamic viscosity of 3.510 mPa·s and surface tension of 35.156 mN/m that satisfy for inkjet printing (**Table S1 and Table S2**). At the optimal solvent ratio, we further prepared the additional two dual-mode fluorescent inks of CSNPs-RB (1.0 wt%) ink and CSNPs-BG (0.8 wt%) ink. The resulting properties (e.g. luminescent brightness, proper dynamic viscosity and surface tension) of these two inks were summarized in **Table S3**.

Fig. 9 demonstrates different complex, dual-mode, multicolored patterns on different paper-based substrates (e.g. a regular A4 paper, envelope, and postcard) in response to different lights. Under daylight, all inkjet printing patterns produced by the three CSNPs inks on different paper-based substrates were invisible. But the encrypted multicolored patterns can be clearly observed under the irradiation of 980 nm laser and 254 nm UV light, respectively. Specifically, a peacock

on a regular A4 paper (**Fig. 9 group A**), a temple on a postcard (**group B**) and a logo of "Hunan University of Technology" on an envelope (**group C**) displayed a clear, complete, and separate multicolored fluorescence districts under 980 nm laser and 254 nm UV light. The multicolored patterns exhibited the almost same fine details in printing (**Fig. S3**). Furthermore, we further selected the CSNPs-GR inks as a typical example and tested its fluorescence stability. Upon exposure of CSNPs-GR inks to ambient surroundings for 15 days, the inks remained the integrity of the fluorescent color both under 980 nm and 254 nm UV light excitation, indicating that no obvious agglomeration of CSNPs-GR nanocomposites was formed (**Fig. S4)**. These results again demonstrate that the CSNPs inks not only are highly compatible with inkjet printing to realize high resolution encryption on different paper-based substrates, but also achieve stable dual-mode UC/DC-responsive emission for enhancing anti-counterfeiting performance.

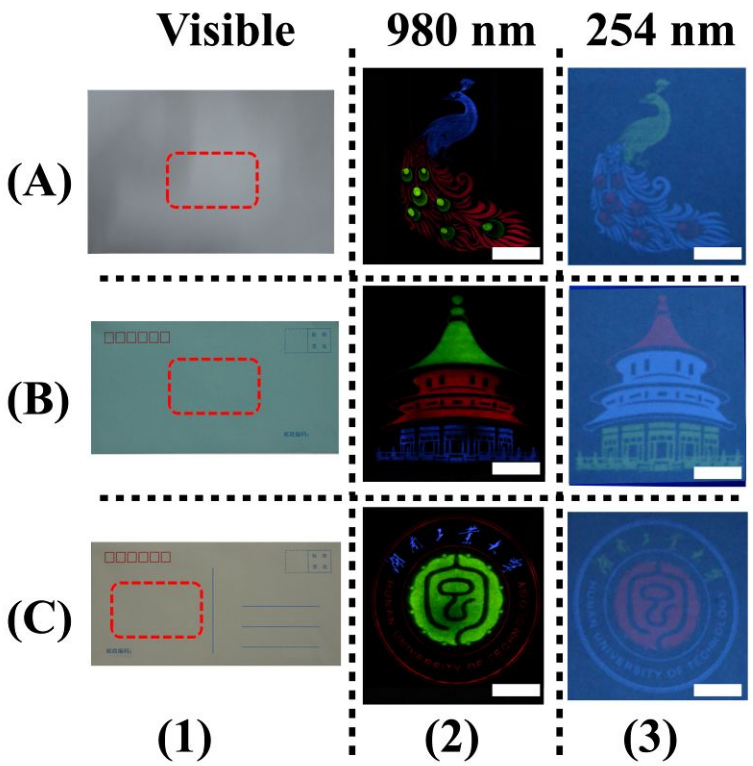

Figure 9. Different inkjet printing patterns using three colored CSNPs inks:, a peacock on a certification (group A), a temple on a postcard (group B) and a logo of "Hunan University of Technology" on an envelope (group C) under visible light (Column 1), a 980 nm laser (Column 2), and a 254 nm UV lamp (Column 3).

4. Conclusions

In this work, mono-dispersed dumbbell-shaped lanthanide-doped $NaYF_4$@$NaGdF_4$ core-shell nanocrystals (CSNPs) with dual-mode fluorescence were successfully synthesized by coating a $NaGdF_4$:Ln'^{3+} shell on a spherical $NaYF_4$:Ln^{3+} core *via* the two-step oleic acid mediated thermal decomposition process. During the CSNP fabrication process, the growth of $NaGdF_4$:Ln'^{3+} shell on the $NaYF_4$:Ln^{3+} nanospherical cores favored the Ostwald ripening growth mechanism, thus inducing CSNPs to change their morphologies from initial nanospheres to intermediate mixtures of nanospheres and many tiny nanoparticles, and ultimately to dumbbell-shaped nanoparticles. Moreover, by tailoring the doped lanthanide ions in the core and shell, CSNPs enabled to realize tunable, multicolor, dual-mode, UC and DC luminescence property under excitation at near-infrared light of 980 nm and ultraviolet light of 254 nm. Finally, CSNPs can be fabricated into water-based, environmental benign luminescent inks and the resultant CSNPs inks are inkjet printed on different paper substrates (A4 paper, postcard, and envelope) to create different, high-resolution image patterns (peacock, temple, and a logo of "Hunan University of Technology"), which are invisible in daylight, but display different UC/DC colors under 980 nm and 254 nm light. Our CSNPs-based fluorescent materials enable the creation of dual-mode light-responsive smart encryption patterns on paper-based substrates in a simple yet secure way, showing a great potential and promising for anti-counterfeiting applications.

Conflicts of interest

The authors declared no competing financial interest.

Acknowledgements

The financial support by National Science Foundation of China (51874129 and 51874128), National Key Research and Development Program of China (No. 2018YFD0400705) and the Natural Science Foundation of Hunan Province (2018JJ3115 and 2019JJ60049) is gratefully acknowledged. J.Z. thanks for financial support from NSF (DMR-1607475 and CMMI-1825122).

References

1. P. Kumar, J. Dwivedi and B. K. Gupta, *J. Mater. Chem. C*, 2014, **2**, 10468-10475.
2. J. Andres, R. D. Hersch, J.-E. Moser and A.-S. Chauvin, *Adv. Funct. Mater.*, 2014, **24**, 5029-5036.
3. M. You, M. Lin, S. Wang, X. Wang, G. Zhang, Y. Hong, Y. Dong, G. Jin and F. Xu, *Nanoscale*, 2016, **8**, 10096-10104.
4. R. Singh, E. Singh and H. S. Nalwa, *RSC Adv.*, 2017, **7**, 48597-48630.
5. H. Peng, S. Bi, M. Ni, X. Xie, Y. Liao, X. Zhou, Z. Xue, J. Zhu, Y. Wei, C. N. Bowman and Y.-W. Mai, *J. Am. Chem. Soc.*, 2014, **136**, 8855-8858.
6. M. Akselrod and J. Kouwenberg, *Radiat. Meas.*, 2018, **117**, 35-51.
7. M. Wang, Y. Xu, H. Tan, L. Xu, C. Zhang and J. Xu, *Nanosci. Nanotechnol. Lett.*, 2018, **10**, 365-372.
8. Y. Zhang, L. Zhang, R. Deng, J. Tian, Y. Zong, D. Jin and X. Liu, *J. Am. Chem. Soc.*, 2014, **136**, 4893-4896.
9. P. Kumar, S. Singh and B. K. Gupta, *Nanoscale*, 2016, **8**, 14297-14340.
10. Y. Zhang, B. Ren, F. Yang, Y. Cai, H. Chen, T. Wang, Z. Feng, J. Tang, J. Xu and J. Zheng, *J. Mater. Chem. C*, 2018, **6**, 11536-11551.
11. H. Tan, S. Xie, N. Li, C. Tong, L. Xu, J. Xu and C. Zhang, *Mater. Express*, 2018, 8, 141-148.

12. H.-Q. Shi, W.-N. Li, L.-W. Sun, Y. Liu, H.-M. Xiao and S.-Y. Fu, *Chem. Commun.*, 2011, **47**, 11921-11923.
13. C. Ji, P. Jiang, X. Ye, M. Chang, F. Liu,Y. Shen, D. Chen, and L. Nie, *Sci. Adv. Mater.*, 2019, **11**, 680-684.
14. K. Jiang, L. Zhang, J. Lu, C. Xu, C. Cai and H. Lin, *Angew. Chem. Int. Edi.*, 2016, **55**, 7231-7235.
15. T. Fan and J. Lu, *Appl. Surf. Sci.*, 2012, **259**, 671-673.
16. C. Zhang, B. Wang, W. Li, S. Huang, L. Kong, Z. Li and L. Li, *Nat. Commun.*, 2017, **8**, 1138.
17. J.-Y. Zou, L. Li, S.-Y. You, Y.-W. Liu, H.-M. Cui, J.-Z. Cui, and S.-W. Zhang, *Dalton Trans.* 2018, **47**, 15694-15702.
18. S. Ning, H. Chen, S. Zhang, P. Cheng, *Polyhedron*, 2018, **155**, 457-463.
19. Y. Han, H. Li, Y. Wang, Y. Pan, L. Huang, F. Song and W. Huang, *Sci. rep.*, 2017, **7**, 1320.
20. D. Gao, X. Zhang, and W. Gao, *ACS Appl. Mater. Interfaces* 2013, **5**, 9732-9739.
21. J. M. Meruga, W. M. Cross, P. Stanley May, Q. Luu, G. A. Crawford and J. J. Kellar, *Nanotechnology*, 2012, **23**, 395201.
22. M. You, J. Zhong, Y. Hong, Z. Duan, M. Lin and F. Xu, *Nanoscale*, 2015, **7**, 4423-4431.
23. L. Zhou, A. Zhao, Z. Wang, Z. Chen, J. Ren and X. Qu, *ACS Appl. Mater. Interfaces*, 2015, **7**, 2905-2911.
24. W. Yao, Q. Tian, J. Liu, Z. Wu, S. Cui, J. Ding, Z. Dai and W. Wu, *J. Mater. Chem. C*, 2016, **4**, 6327-6335.
25. J. M. Meruga, A. Baride, W. Cross, J. J. Kellar and P. S. May, *J. Mater. Chem. C*, 2014, **2**, 2221-2227.
26. B. Song, H. Wang, Y. Zhong, B. Chu, Y. Su and Y. He, *Nanoscale*, 2018, **10**, 1617-1621.
27. L. L. da Luz, R. Milani, J. F. Felix, I. R. B. Ribeiro, M. Talhavini, B. A. D. Neto, J. Chojnacki, M. O. Rodrigues and S. A. Júnior, *ACS Appl. Mater. Interfaces*, 2015, **7**, 27115-27123.
28. P. Qiu, N. Zhou, H. Chen, C. Zhang, G. Gao and D. Cui, *Nanoscale*, 2013, **5**, 11512-11525.
29. G. Wang, Q. Peng and Y. Li, *Acc. Chem. Res.*, 2011, **44**, 322-332.
30. G. Chen, C. Yang and P. N. Prasad, *Acc. Chem. Res.*, 2013, **46**, 1474-1486.

31. H. Tan, S. Xie, J. Xu, N. Li, C. Zhang, L. Xu and J. Zheng, *Sci. Adv. Mater.*, 2017, **9**, 2223-2233.
32. Y. Wu, C. Li, D. Yang and J. Lin, *J. Colloid Interface Sci.*, 2011, **354**, 429-436.
33. H. Dong, L.-D. Sun and C.-H. Yan, *Chem. Soc. Rev.*, 2015, **44**, 1608-1634.
34. S. Xie, C. Tong, H. Tan, N. Li, L. Gong, J. Xu, L. Xu and C. Zhang, *Mater. Chem. Front.*, 2018, **2**, 1997-2005.
35. J.-C. Boyer, F. Vetrone, L. A. Cuccia and J. A. Capobianco, *J. Am. Chem. Soc.*, 2006, **128**, 7444-7445.
36. W. Niu, S. Wu, S. Zhang, J. Li and L. Li, *Dalton Trans.*, 2011, **40**, 3305-3314.
37. P. Kumar, J. Dwivedi and B. K. Gupta, *J. Mater. Chem. C*, 2014, **2**, 10468-10475.
38. S. K. Singh, A. K. Singh and S. B. Rai, *Nanotechnology*, 2011, **22**, 275703.
39. Kanika, P. Kumar, S. Singh and B. K. Gupta, *Chem. Eur. J.*, 2017, **23**, 17144-17151.
40. M. Li, W. Yao, J. Liu, Q. Tian, L. Liu, J. Ding, Q. Xue, Q. Lu and W. Wu, *J. Mater. Chem. C*, 2017, **5**, 6512-6520.
41. S. Xu, Y. Yu, Y. Gao, Y. Zhang, X. Li, J. Zhang, Y. Wang and B. Chen, *Microchim. Acta*, 2018, **185**, 454.
42. Y. Liu, K. Ai and L. Lu, *Nanoscale*, 2011, **3**, 4804-4810.
43. P. P. Sukul, M. K. Mahata and K. Kumar, *J. Lumin.*, 2017, **185**, 92-98.
44. H. Li, G. Liu, J. Wang, X. Dong and W. Yu, *J. Colloid Interface Sci.*, 2017, **501**, 215-221.
45. L. Wang, H. Chen, D. Zhang, D. Zhao and W. Qin, *Mater. Lett.*, 2011, **65**, 504-506.
46. H.-X. Mai, Y.-W. Zhang, R. Si, Z.-G. Yan, L.-D. Sun, L.-P. You and C.-H. Yan, *J. Am. Chem. Soc.*, 2006, **128**, 6426-6436.
47. X. Teng, Y. Zhu, W. Wei, S. Wang, J. Huang, R. Naccache, W. Hu, A. I. Y. Tok, Y. Han, Q. Zhang, Q. Fan, W. Huang, J. A. Capobianco and L. Huang, *J. Am. Chem. Soc.*, 2012, **134**, 8340-8343.
48. S. Zeng, G. Ren, C. Xu and Q. Yang, *CrystEngComm*, 2011, **13**, 1384-1390.
49. D. Xie, H. Peng, S. Huang and F. You, *J. Nanomaterials*, 2013, **2013**, 4-4.
50. Y. Liu, D. Tu, H. Zhu, R. Li, W. Luo and X. Chen, *Adv. Mater.*, 2010, **22**, 3266-3271.
51. M. Ding, D. Chen, Z. Wan, Y. Zhou, J. Zhong, J. Xi and Z. Ji, *J. Mater. Chem. C*, 2015, **3**, 5372-5376.

52. W. Yao, Q. Tian, B. Tian, M. Li, H. Wang, P. Zeng, L. Liu, H. Zheng and W. Wu, *Sci. China Mater.*, 2019, **62**, 368-378.

53. C. Liu, H. Wang, X. Li and D. Chen, *J. Mater. Chem.*, 2009, **19**, 3546-3553.

54. H. Na, K. Woo, K. Lim and H. S. Jang, *Nanoscale*, 2013, **5**, 4242-4251.

55. N. Bogdan, F. Vetrone, G. A. Ozin and J. A. Capobianco, *Nano Lett.*, 2011, **11**, 835-840.

56. B. Zhou, L. Tao, Y. Chai, S. P. Lau, Q. Zhang and Y. H. Tsang, *Angew. Chem. Int. Edi.*, 2016, **55**, 12356-12360.

57. Z. Yu, H. Zhou, G. Zhou, J. Zhou, Y. Wu, X. Zhang, T. Wang, D. Huang, X. Wang and J. Hu, *Phys. Chem. Chem. Phys.*, 2017, **19**, 31675-31683.

58. F. Wang, R. Deng and X. Liu, *Nat. Protoc.*, 2014, **9**, 1634.

59. B. Voß, J. Nordmann, A. Uhl, R. Komban and M. Haase, *Nanoscale*, 2013, **5**, 806-812.

60. H.-Q. Wen, H.-Y. Peng, K. Liu, M.-H. Bian, Y.-J. Xu, L. Dong, X. Yan, W.-P. Xu, W. Tao, J.-L. Shen, Y. Lu and H.-S. Qian, *ACS Appl. Mater. Interfaces*, 2017, **9**, 9226-9232.

61. B.-B. Ding, H.-Y. Peng, H.-S. Qian, L. Zheng and S.-H. Yu, *Adv. Mater. Interfaces*, 2016, **3**, 1500649.

62. F. Vetrone, R. Naccache, V. Mahalingam, C. G. Morgan and J. A. Capobianco, *Adv. Funct. Mater.*, 2009, **19**, 2924-2929.

63. Y. Wang, L. Tu, J. Zhao, Y. Sun, X. Kong and H. Zhang, *J. Phys. Chem. C*, 2009, **113**, 7164-7169.

64. J. A. Damasco, G. Chen, W. Shao, H. Ågren, H. Huang, W. Song, J. F. Lovell and P. N. Prasad, *ACS Appl. Mater. Interfaces*, 2014, **6**, 13884-13893.

65. X. Huang, *Dyes Pigm.*, 2016, **130**, 99-105.